# Nonlinear Photon Sieves for High-Fidelity Wavefront Engineering

*Jia-chen Yang, Wei Chen,\* Ling-ling Ma,\* An-zhuo Yu, Jin-tao Pan, Jin-tao Fan,\* Ming-lie Hu, and Yan-qing Lu\**

Domain-engineered nonlinear photonic crystals have long served as versatile platforms for structured light modulation, leveraging spatially dependent nonlinearity to control the wavefronts of nonlinear interacting waves. However, most of these crystals rely on classical nonlinear holography, which is limited to unidirectional light field reconstruction and suffers from mode degradation caused by fabrication imperfections, such as lateral domain diffusion. Here, nonlinear photon sieves that replace the stripe-like patterns with discrete dot-array structures are introduced. This design not only exhibits high noise resistance but also enables multidimensional, high-fidelity modulation of nonlinear structured light. This experiments demonstrate the nonlinear generation of Airy beams, higher-order Laguerre–Gaussian beams, Hermite–Gaussian beams, and Ince–Gaussian beams across a broadband spectrum from 450 to 650 nm. This approach provides a robust, multidimensional platform for the development of domain-engineered nonlinear photonic crystals, opening new avenues for advanced optical modulation and computation.

## 1. Introduction

Structured light—characterized by its unique wavefront (amplitude, phase, and polarization, etc.)—plays a crucial role in diverse important fields such as optical manipulation, materials processing, and optical communication.[1–5] Simultaneously, nonlinear light-matter interactions offer an efficient route to convert fixed-wavelength beams into desired frequencies, thereby enabling more flexible and tunable structured light sources.[6,7] Interestingly, various structured light beams can interact within

J.-C. Yang, W. Chen, L.-L. Ma, A.-Z. Yu, J.-T. Pan, Y.-Q. Lu
Key Laboratory of Intelligent Optical Sensing and Manipulation, College Engineering and Applied Sciences, Collaborative Innovation Center of Advanced Microstructures, National Laboratory of Solid State Microstructures
Nanjing University
Nanjing 210093, China
E-mail: wchen@nju.edu.cn; malingling@nju.edu.cn; yqlu@nju.edu.cn
J.-T. Fan, M.-L. Hu
School of Precision Instruments and Opto-electronics Engineering, Key Laboratory of Opto-electronic Information Science and Technology of Ministry of Education, Ultrafast Laser Laboratory
Tianjin University
Tianjin 300072, China
E-mail: fanjintao@tju.edu.cn

nonlinear media, allowing more intricate modulation of both the nonlinear beam's frequency and wavefront,[2,7] which in turn drives progress in emerging applications that leverage nonlinear optical phenomena and structured light, such as nonlinear optical computing and nonlinear optical neural networks.[8–10]
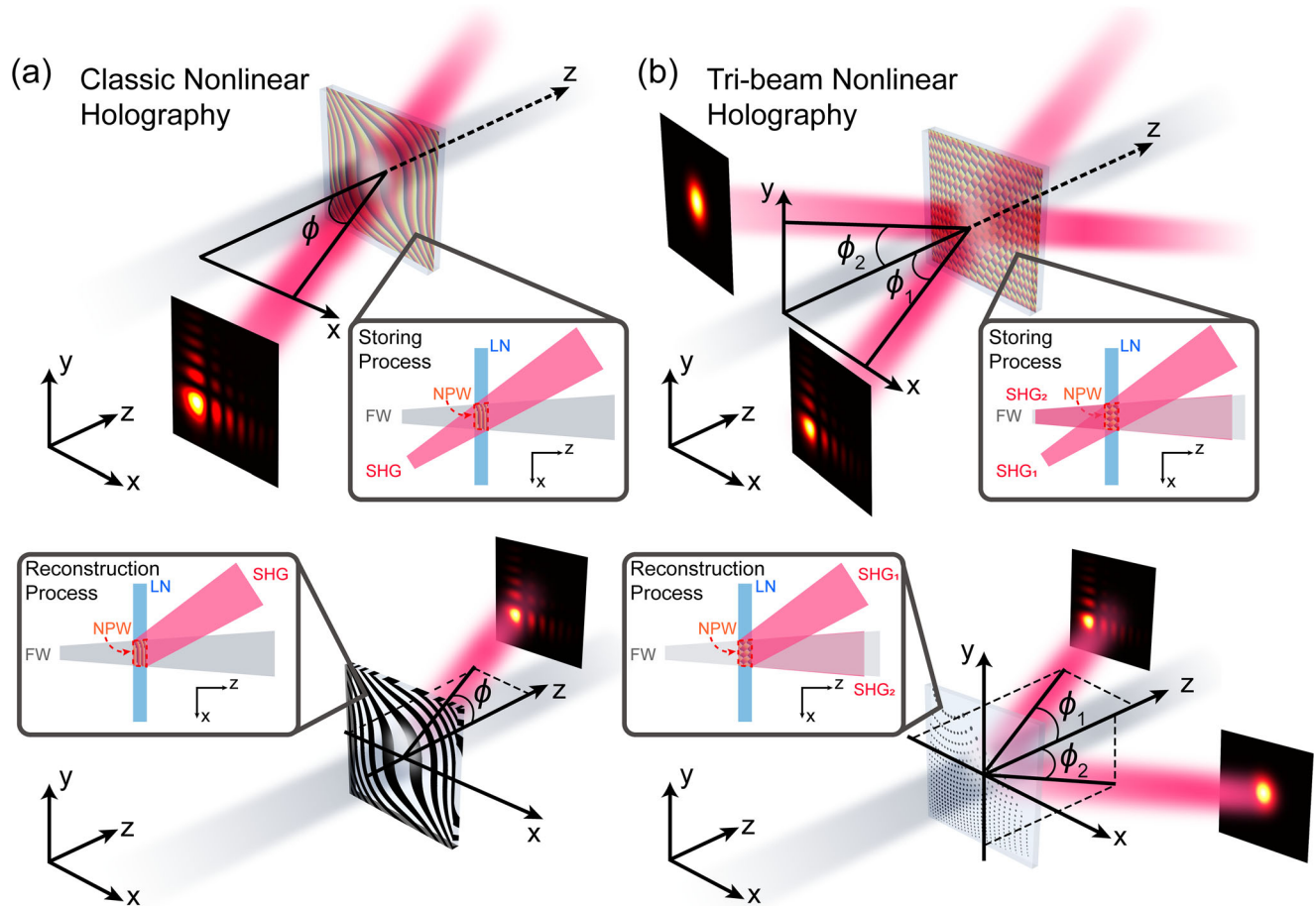
Concurrently, metasurfaces have attracted considerable interest due to their effective wavefront control capabilities in both linear and nonlinear regimes. Their tailored nanostructures permit extensive manipulation of optical wavefronts, while recent advances in nonlinear metasurfaces extend this control across multiple frequency bands through processes such as second- or third-harmonic generation.[11–18] However, scalability issues persist for metasurfaces, as subwavelength lithography on millimeter- or centimeter-scale areas remains expensive and technologically challenging.[19] By contrast, domain-engineered ferroelectric nonlinear optical crystals (e.g., $LiNbO_3$ (LN) and $KTiOPO_4$ (KTP)) have long provided large-area solutions for nonlinear frequency conversion via quasi-phase-matching.[20] Indeed, periodically poled $LiNbO_3$ (PPLN) is widely employed in second-harmonic generation for commercial laser applications.[20] Methods such as electric-field poling enable domain structures ranging from hundreds of micrometers to centimeters, offering a cost-effective route to high-power, large-aperture nonlinear processes. Nonetheless, such domain-engineered ferroelectrics have long lagged in achieving the precise wavefront control exhibited by both linear and nonlinear metasurfaces.[21–25]

Recent advances in 3D laser direct writing of ferroelectric crystals have introduced a paradigm shift, enabling the fabrication of multilayered, intricately engineered domain structures with submicron precision.[26–31] However, most efforts in this direction still rely on classical "nonlinear holography", which typically yields stripe-like domain patterns.[22,23] These stripe-like configurations inherently restrict beam shaping to a single axis ($x$ or $y$) and suffer from fabrication-induced errors such as domain diffusion and mechanical vibrations. As a result, the exploration of high-dimensional, multi-channel wavefront engineering in conventional nonlinear photonic crystals has been substantially limited.[22,23,32]

**Figure 1.** From classical nonlinear holography to tri-beam nonlinear holography. Schematics of the storing and reconstruction processes in a) classical nonlinear holography and proposed b) tri-beam nonlinear holography.

Here, we propose nonlinear photon sieves by introducing a tri-beam nonlinear holography that transforms conventional stripe-like domain patterns into dot-like domains. This approach enables independent control of structured light along both the $x$ and $y$ axes while ensuring high noise resistance. As a proof of concept, our method generates a broad range of structured beams at the second-harmonic (SH) frequency with high fidelity (>90%), including Airy, higher-order Laguerre-Gaussian (LG), Hermite-Gaussian (HG), and Ince-Gaussian (IG) beams. These nonlinear photon sieves also allow for the independent creation of distinct beam profiles along orthogonal directions. Additionally, by leveraging the broadband characteristics of three-wave mixing in these structures, we achieve multi-wavelength structured beam generation from 450 nm to 650 nm, underscoring the versatility of our approach. These results open a promising avenue for domain-engineered nonlinear optical crystals, with potential applications in optical manipulation, optical computing, and beyond.

## 2. From Classical Nonlinear Holography to Tri-Beam Nonlinear Holography

Before discussing the tri-beam nonlinear holography, we first re-examine the classical nonlinear holography technique.[22,23] Tak-

ing the generation of an SH Airy beam as an example (**Figure 1a**), classical nonlinear holography involves two processes: storing and reconstruction. In the storing process, the holographic pattern is formed by the interference of a nonlinear polarization wave (NPW) beam (usually simplified as a plane wave) excited by the fundamental wave (FW) beam and an SH beam at an angle $\phi$ (along the $x$-axis) to the propagation direction $z$. Typically, the FW beam is perpendicular to the nonlinear crystal, i.e., $\boldsymbol{E}_{\mathrm{FW}} = A_{\mathrm{FW}} \exp(-ik_1 z)\hat{\boldsymbol{u}}_p$, where $A_{\mathrm{FW}}$ represents the complex amplitude of the FW wave (Gaussian beam in our experiment), $\hat{\boldsymbol{u}}_p$ is the unit vector which represents the polarization direction of the optical fields, $k_1 = \frac{2\pi}{\lambda_1}$ is the wavenumber, and $\lambda_1$ is the wavelength. To simplify the analysis and focus on the spatial distributions of the light fields, we assume that both the incident fundamental wave and the generated SH beam are linearly polarized in the same direction (denoted by the unit vector $\hat{\boldsymbol{u}}_p$). This condition can be easily achieved in experiments by adjusting the polarization angle of the incident linearly polarized light.[6] Therefore, the generated NPW can be expressed as $\boldsymbol{E}_p = A_p \exp(-ik_2 z)\hat{\boldsymbol{u}}_p$, where the $A_p$ is assumed to be real, considering the FW wave is a Gaussian beam, with $k_2 = 2k_1$ due to momentum conservation in an SH process. The SH beam (the target structured light) can be represented as $\boldsymbol{E}_s = A_s \exp[-ik_2 z - ik_2 \sin(\phi)x]\hat{\boldsymbol{u}}_p$, where $A_s$ is the

ADVANCED
SCIENCE NEWS

www.advancedsciencenews.com

LASER
& PHOTONICS
REVIEWS

www.lpr-journal.org

complex amplitude distribution of the target structured light and $\phi$ is the previously mentioned angle between the FW beam and the SH beam. One can find that the interference between the FW beam and the SH beam can be expressed as:

$$I(x, y) = \left| E_p + E_s \right|^2$$

$$= \left| E_p \right|^2 + \left| E_s \right|^2 + E_p^* \cdot E_s + E_p \cdot E_s^*$$

$$= \left| E_p \right|^2 + \left| E_s \right|^2 + 2\mathrm{Re} \left\{ A_p^* A_s \exp \left[ -ik_2 \sin(\phi) x \right] \right\}. \quad (1)$$

Then, ignoring the background signal $I_0 = |E_p|^2 + |E_s|^2$, we focus on the remaining term $I_1 = 2\mathrm{Re}\{A_p^* A_s \exp[-ik_2 \sin(\phi)x]\}$. Subsequently, we impose $I_1$ in the nonlinear crystal. Since the quadratic nonlinear coefficient $\chi^{(2)}$ is in a binary format with only two possible values, either $d_{ij}$ or $-d_{ij}$, where $d_{ij}$ is the element of the quadratic susceptibility, the structure function $f(x, y)$ of the required nonlinear photonic crystal can be expressed as $f(x, y) = \mathrm{sgn}\{I_1\}$. Through a Fourier-Taylor expansion, one can see that the above nonlinear modulation function $f(x, y)$ exhibits the dominant $\pm 1$-order component:

$$f_{\pm 1}(x, y) = A_p^* A_s \exp \left[ -ik_2 \sin(\phi) x \right] + A_p A_s^* \exp \left[ +ik_2 \sin(\phi) x \right] \quad (2)$$

In the reconstruction process, we let an FW beam incident perpendicular to the nonlinear crystal. Therefore, the final nonlinear diffracted field $E_r$ modulated by $f_{\pm 1}(x, y)$ can be expressed as:

$$E_r = f_{\pm 1}(x, y) E_p = f_{\pm 1}(x, y) A_p \exp(-ik_2 z) \hat{u}_p$$

$$= A_p^* A_p A_s \exp \left[ -ik_2 z - ik_2 \sin(\phi) x \right] \hat{u}_p$$

$$+ A_p A_p^* A_s^* \exp \left[ -ik_2 z + ik_2 \sin(\phi) x \right] \hat{u}_p$$

$$= A_p^2 E_s + A_p^2 E_s^{conj} \exp(-2ik_2 z)$$

$$= A_p^2 E_s + E_p^2 E_s^{conj}, \quad (3)$$

where $E_p^2 = A_p^2 \exp(-2ik_2 z)$, and $A_p = A_p^*$ (since $A_p$ is real). Equation (3) shows that $E_r$ indeed realizes the reconstruction of the target structured light $E_s$, which propagates at an angle $\phi$ relative to the $z$-axis in the $x$-direction. Simultaneously, its conjugate beam, $E_p^2 E_s^{conj} = A_p^2 A_s^* \exp[-ik_2 z + ik_2 \sin(\phi)x]\hat{u}_p$ is also generated, whose complex amplitude distribution $A_s^*$ is the complex conjugate of $A_s$ a(the complex amplitude distribution of $E_s$), and the propagation direction of this beam forms an angle of $-\phi$ respect to the $z$-axis along the $x$ direction. It is worth noting that the obtained nonlinear photonic crystal usually exhibits quasi-periodic (stripe) structures perpendicular to the $x$-axis due to the angle information between the FW beam and the SH beam (see Equation (1) and Figure 1a).

Next, we turn to the proposed tri-beam nonlinear holography. Inspired by linear multi-beam holography,[33] we recognize that the classical nonlinear holography discussed above lacks modulation along the $y$-axis, whereas the latter can carry independent modulation (information) due to its orthogonality to the $x$-axis. More specifically, in the storing process, the SH beam (the target structured light) could be designed as the superposition of two

independent structured lights at angles $\phi_1$ and $\phi_2$ with respect to the FW beam in the $x$ and $y$ directions, respectively, i.e.,

$$E_s' = E_{s1} + E_{s2},$$
$$E_{s1} = A_{s1} \exp \left[ -ik_2 z - ik_2 \sin(\phi_1) x \right] \hat{u}_p, \quad (4)$$
$$E_{s2} = A_{s2} \exp \left[ -ik_2 z - ik_2 \sin(\phi_2) y \right] \hat{u}_p,$$

where $A_{s1}$ and $A_{s2}$ being the complex amplitudes of the two independent structured lights. Therefore, the interference between the FW beam and the SH beam can be expressed as:

$$I'(x, y) = \left| E_p + E_s' \right|^2$$

$$= \left| E_p \right|^2 + \left| E_{s1} \right|^2 + \left| E_{s2} \right|^2$$

$$+ 2\mathrm{Re} \left\{ A_p^* A_{s1} \exp \left[ -ik_2 \sin(\phi_1) x \right] \right\}$$

$$+ 2\mathrm{Re} \left\{ A_p^* A_{s2} \exp \left[ -ik_2 \sin(\phi_2) y \right] \right\}$$

$$+ 2\mathrm{Re} \left\{ A_{s1} A_{s2}^* \exp \left[ -ik_2 \sin(\phi_1) x + ik_2 \sin(\phi_2) y \right] \right\} \quad (5)$$
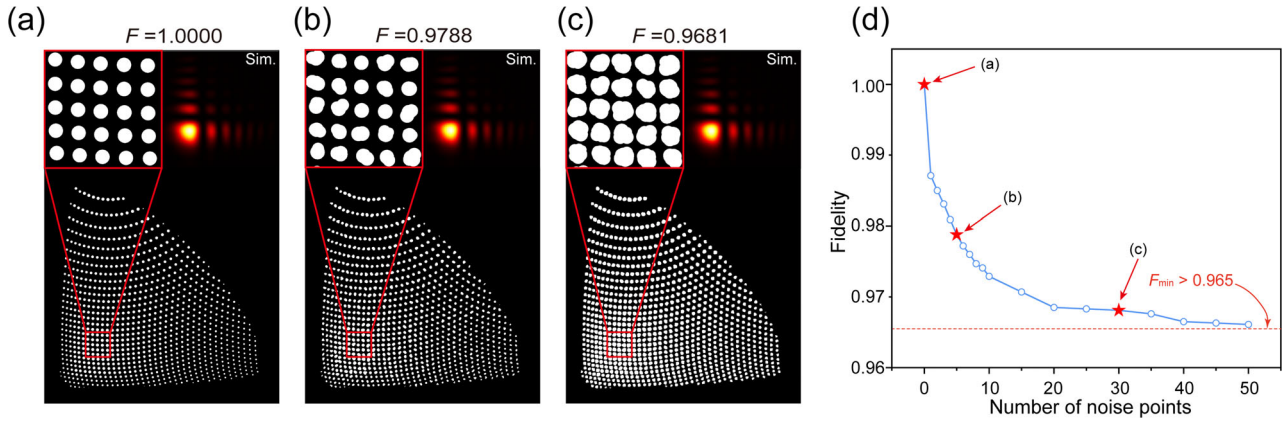
Next, we ignore the direct current term $I_0' = |E_p|^2 + |E_{s1}|^2 + |E_{s2}|^2$ in $I'(x, y)$ and fabricate the nonlinear crystal based on $f'(x, y) = \mathrm{sgn}\{I_1'\}$, where $I_1' = 2\mathrm{Re}\{A_p^* A_{s1} \exp[-ik_2 \sin(\phi_1)x]\} + 2\mathrm{Re}\{A_p^* A_{s2} \exp[-ik_2 \sin(\phi_2)y]\}$. It is noteworthy that we also ignore the cross-modulation term $2\mathrm{Re}\{A_{s1}A_{s2}^* \exp[-ik_2 \sin(\phi_1)x + ik_2 \sin(\phi_2)y]\}$. Similarly, $f'(x, y)$ exhibits the dominant $\pm 1$-order component that could be expressed as:

$$f_{\pm 1}'(x, y) = A_p^* A_{s1} \exp \left[ -ik_2 \sin(\phi_1) x \right]$$

$$+ A_p^* A_{s2} \exp \left[ -ik_2 \sin(\phi_2) y \right]$$

$$+ A_p A_{s1}^* \exp \left[ +ik_2 \sin(\phi_1) x \right]$$

$$+ A_p A_{s2}^* \exp \left[ +ik_2 \sin(\phi_2) y \right]. \quad (6)$$

When an FW beam is incident perpendicular to the nonlinear crystal modulated by $f_{\pm 1}'(x, y)$, the resulting final nonlinear diffracted field $E_r'$ can be obtained:

$$E_r' = f_{\pm 1}'(x, y) E_p = f_{\pm 1}'(x, y) A_p \exp(-ik_2 z)\hat{u}_p$$

$$= A_p^* A_p A_{s1} \exp \left[ -ik_2 z - ik_2 \sin(\phi_1)x \right] \hat{u}_p$$

$$+ A_p^* A_p A_{s2} \exp \left[ -ik_2 z - ik_2 \sin(\phi_2)y \right] \hat{u}_p$$

$$+ A_p A_p^* A_{s1}^* \exp \left[ -ik_2 z + ik_2 \sin(\phi_1)x \right] \hat{u}_p$$

$$+ A_p A_p^* A_{s2}^* \exp \left[ -ik_2 z + ik_2 \sin(\phi_2)y \right] \hat{u}_p$$

$$= A_p^2 (E_{s1} + E_{s2}) + E_p^2 \left( E_{s1}^{conj} + E_{s2}^{conj} \right). \quad (7)$$

One sees clearly that the nonlinear diffracted field $E_r'$ reconstructs two independent target structured lights ($E_{s1}$ and $E_{s2}$),

**ADVANCED
SCIENCE NEWS**

www.advancedsciencenews.com

LASER
& PHOTONICS
REVIEWS

www.lpr-journal.org

**Figure 2.** Ideal and noise-added nonlinear photon sieves holograms for generating an Airy beam. a) Ideal design of Airy beam tri-beam nonlinear hologram and its diffracted field. b) Airy beam tri-beam nonlinear hologram with five added noise points. c) Airy beam tri-beam nonlinear hologram with thirty added noise points. d) The function showing the fidelity variation as the number of noise points increases, with points corresponding to (a), (b), and (c) highlighted.

with propagation directions having angles $\phi_1$ and $\phi_2$ with respect to the $z$-axis along the $x$ and $y$ directions respectively. Simultaneously, two conjugate beams are generated at angles $-\phi_1$ and $-\phi_2$, analogous to the case in classical nonlinear holography. More importantly, the resulting nonlinear photonic crystal transforms to a rhombus-like structure in the $x - y$ plane due to the angle information of the FW beam and the SH beam along the $x$ and $y$ axes (see Equation (5) and Figure 1b). In Figure 1b, we demonstrate a nonlinear photon sieve obtained through our proposed scheme, capable of generating an Airy beam and a Gaussian beam in the $x$ and $y$ directions, respectively.

Furthermore, since the $x$ and $y$ directions can be independently modulated, one can also superimpose lens phases with different focal lengths $f_{lens}$ either the $x$ or $y$ direction as:

$$\phi_{lens}\left(x, y, f_{lens}\right) = -\frac{2\pi}{\lambda}\left[\left(x^2 + y^2\right) / \left(2f_{lens}\right)\right] \tag{8}$$

thereby reconstructing the target light field at a set position (Fourier plane). Conversely, the conjugate beams undergo a defocusing effect induced by the lens phase, resulting in their suppression at this focal plane. Comparing with the classical nonlinear holography which can only generate diffracted field in one single direction, the tri-beam nonlinear holography we proposed takes advantage of two structured lights along both $x$ and $y$ axes, and can be reconstructed in adjustable distances and directions with relative low crosstalk between each other and the FW, exploring the new dimension in nonlinear holography.

## 3. Nonlinear Photon Sieves and Their High Noise Resistance

Notably, the tri-beam nonlinear holography method yields a hologram formed by a discrete array of rhombus-like elements with size variations, rather than the stripe-like patterns typical of classical nonlinear holography. This design inherently provides strong resistance to the fabrication errors commonly encountered in nonlinear photonic crystals (see Figures S1 and S2, Supporting Information for further details). Based on this, we trans-

form the near-rhombus features in the original hologram with circular dots that preserve the same center and area, thereby producing a nonlinear version of the photon sieve.[33–36]

To provide a specific example, we simulate the diffracted fields from both ideal and noise-added nonlinear photon sieves engineered to generate an Airy beam (shown in **Figure 2**). In this ideal design, the black and white regions represent the modulation of different signs in the domains of a nonlinear crystal, and the elementary units in the pattern are standard circular shapes. To simulate fabrication imperfections, noise is introduced into the circular-dot areas based on the following principle (see Figure S3, Supporting Information for details): noise points are distributed uniformly within a circular region centered on each original dot, with their radius randomly selected from a continuous uniform distribution in the range [0, $1.5R_{dot}$], where $R_{dot}$ is the radius of the original dot. Meanwhile, the area of each noise point is sampled from a continuous uniform distribution in $(0, 0.5A_{dot}]$, where $A_{dot}$ is the area of the original dot. This design simulates practical fabrication defects such as local overgrowth or edge roughness around the dots, with noise points ranging in size from negligible to half the area of the original dot. This method results in irregularly shaped dots, closely mimicking the real tri-beam nonlinear holograms fabricated in experiments (see Figure 3c in the main text). Noise-added holograms with five and thirty noise points are shown in Figure 2b,c, respectively. Despite noticeable transformations in the shape and linewidth of the dots compared with the original design, no visible changes are observed in the corresponding diffracted fields.

We calculate the fidelity $F$ to quantify the similarity between the diffracted fields of noise-added holograms and the ideal design,

$$F = \left|\frac{\int U(m, n) V^*(m, n)\, dmdn}{\sqrt{\int |U(m, n)|^2 dmdn \int |V(m, n)|^2 dmdn}}\right|^2, \tag{9}$$

where $U(m, n)$ and $V(m, n)$ are the 2D functions being compared (either in real space or Fourier space). In this analysis, the

**ADVANCED
SCIENCE NEWS**

www.advancedsciencenews.com

**LASER
& PHOTONICS
REVIEWS**

www.lpr-journal.org

diffracted field of the original tri-beam nonlinear hologram with standard circular dots (Figure 2a) is taken as the target complex field $U(x, y)$, while the diffracted field of the noise-added hologram is considered the actual complex field $V(x, y)$. Using this method, the fidelities of the diffracted fields for the noise-added holograms in Figure 2b (five noise points) and Figure 2c (thirty noise points) are determined to be $F = 0.9788$ and $F = 0.9681$, respectively.

To examine the broader relationship between fidelity and the number of noise points, additional simulations are conducted. As shown in Figure 2d, an increase in the number of noise points leads to a gradual reduction in fidelity. However, even with as many as 50 noise points, the fidelity of the diffracted field remains above $F_{min} > 0.965$, demonstrating the excellent noise immunity of tri-beam nonlinear holograms. The fidelities of the diffracted fields shown in Figures 2a–c are highlighted in the line chart for comparison. These analyses clearly demonstrate that the dots of tri-beam nonlinear holograms can be transformed into irregular shapes—facilitating practical fabrication—without significantly degrading the quality of the diffracted field. The diffracted fields maintain high fidelity compared with the original design, effectively overcoming manufacturing imperfections.

## 4. Experimental Results

We thereby carry out experiments to validate the capability of high-fidelity wavefront engineering using nonlinear photon sieves. **Figure 3a** shows the schematic of the experimental setup. The FW beam, generated by a Ti:sapphire femtosecond laser (Revolution, Coherent, USA) pumping an optical parametric amplifier (TOPAS-Prime, Light Conversion, Lithua-

nia), has a pulse width of 50 fs and a repetition rate of 1 kHz. For this experiment, we set the wavelength to 1300 nm and use an attenuation pad to adjust the energy. The FW is spatially filtered, expanded, and collimated using two spherical lenses ($f = 200$ mm and 500 mm), combined with a pinhole at the Fourier plane of the $4f$ configuration. Long-pass and short-pass filters block residual FW and unwanted wavelengths.

We first generate the SH Airy beam, with the corresponding nonlinear photon sieve designed using angles $\phi_1 = \phi_2 = 1°$ (according to Equation (5)), and a focal length for Airy beam and Gaussian beam of $f_{lens1} = 200$ mm and $f_{lens2} = 100$ mm (according to Equation (8)). These parameters allow the creation of periodic photon sieves with suitable linewidths, facilitating fabrication in the nonlinear crystal and high-contrast resolvable light fields. Using the electric-field poling method, we encode the designed nonlinear holographic masks onto a LN slice (details of the fabrication process for the pattern-poled LN are provided in Figure S4, Supporting Information).

When the FW illuminates the LN-Airy mask, an SH Airy beam is focused at the designed focal distance of $d = f_{lens1} = 200$ mm, with the wavelength converted from the invisible 1300 nm FW to the visible 650 nm SH, as shown in Figure 3b (see the defocusing conjugate beam in Figure S6, Supporting Information). The co-generated Gaussian beam is shown in Figure S7a (Supporting Information). With the assistance of an aspheric lens ($f = 45$ mm), we clearly image the fabricated domain structure (Figure 3c), where the black circles represent the domain walls of opposite polarization directions. Despite imperfections in the domain walls due to fabrication limitations, theoretical analysis confirms that these flaws have less impact on the diffracted field due to the strong noise-resistance of the nonlinear photon sieve. This robustness is further evidenced by the high similarity between simulation and experimental results. The propagation dynamics of the SH Airy beam, analyzed in Figure 3d, exhibit the characteristic self-acceleration behavior.

Based on a similar design principle, we encode additional nonlinear photon sieves onto LN slices to generate various SH structured light fields. Simulated and experimental results for nonlinear photon sieves generating a high order LG mode, a petal pattern resulting from the superposition
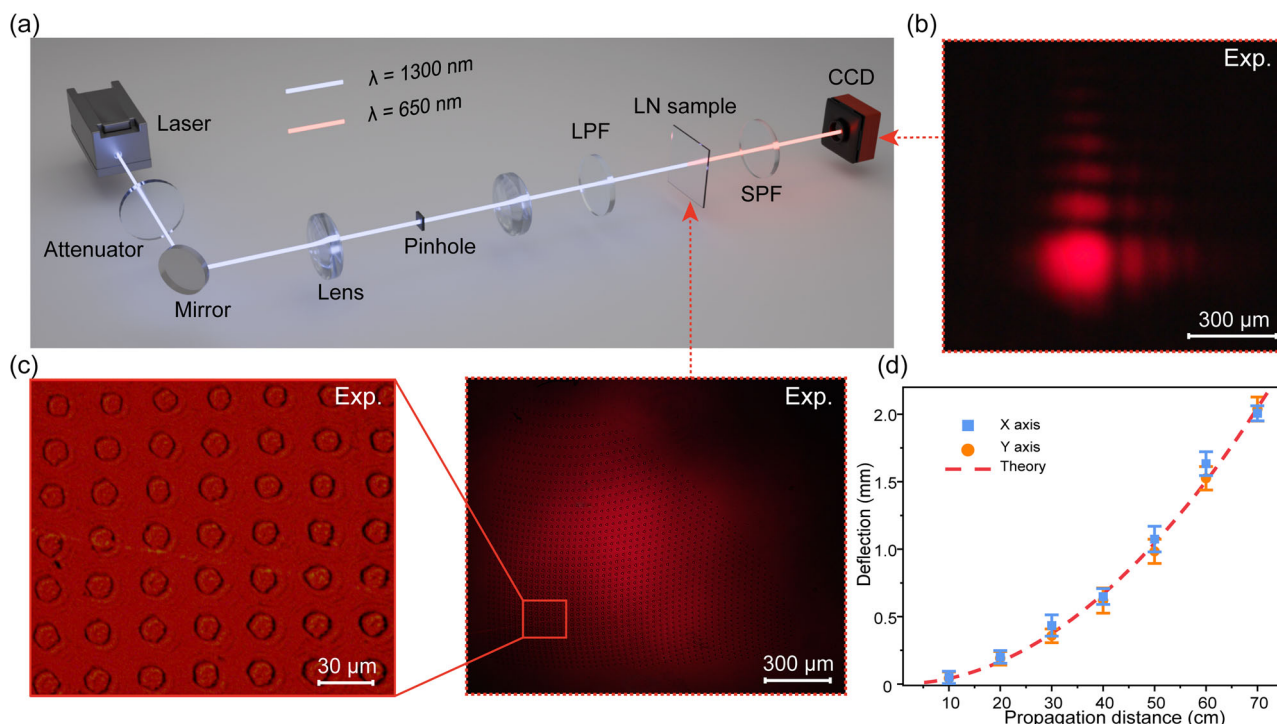


**Figure 3.** Experimental demonstration of a nonlinear photon sieve generating an SH Airy beam. a) Schematic of experimental setup for SH Airy beam generation. b) Experimentally observed SH Airy beam. c) Surface of the pattern poled LN to generate Airy beam. d) Propagation dynamics of SH Airy beam.
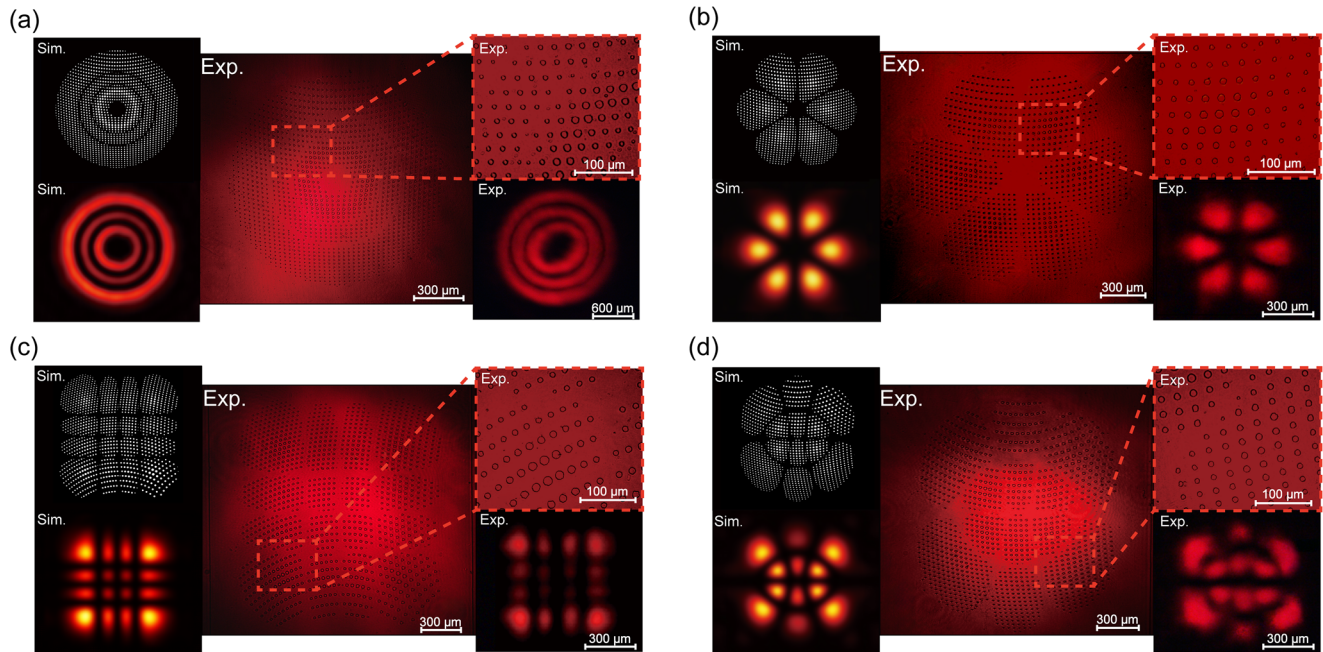
**Figure 4.** Simulation and experimental results for tri-beam nonlinear holograms generating various nonlinear structured lights. a) LG beam with vortex charge of $l = 5$ and radial mode of $p = 2$. b) Superposition state of two LG beams with opposite vortex charges $l = \pm 3$ and $p = 0$. c) HG beam with mode orders of $m = 3$ and $n = 3$. d) Odd IG beam of the order $p = 5$ and degree $m = 3$.

of two LG beams, a high order HG mode, and a more complex IG mode (as shown in **Figure 4**), and the co-generated Gaussian beams with these structured lights are shown in Figure S7b–e (Supporting Information). Note that the generated LG beam is wider than other beams in order to coordinate the size of photon sieves. The circular-dot distributions closely match the amplitude of the desired beams, owing to the stable intensity profiles during beam propagation. Thanks to the nonlinear photon sieves design, the minimum linewidth of the circular dots significantly exceeds the resolution limit of the lithography machine used to fabricate the hologram mask. This ensures that almost any type of structured light can be generated with high fidelity in the SH process. In contrast, classical nonlinear holography, characterized by stripe-structured holograms, is inherently limited by its weak resistance to fabrication noise, often resulting in the generation of only low-order LG and HG modes.[37,38] While recent experiments have demonstrated the generation of IG modes,[39] the beam quality remains below the fidelity achieved with our approach.

To substantiate the higher noise resistance of the photon sieve over strip-based nonlinear holograms, we perform comparative simulations under two typical fabrication noise scenarios: random dot removal and positional offset. Our results show that, for both types of noise, the photon sieve retains far-field fidelity above 0.8, whereas the strip-based pattern rapidly degrades below 0.3 under equivalent conditions (see Section S6, Supporting Information for details).
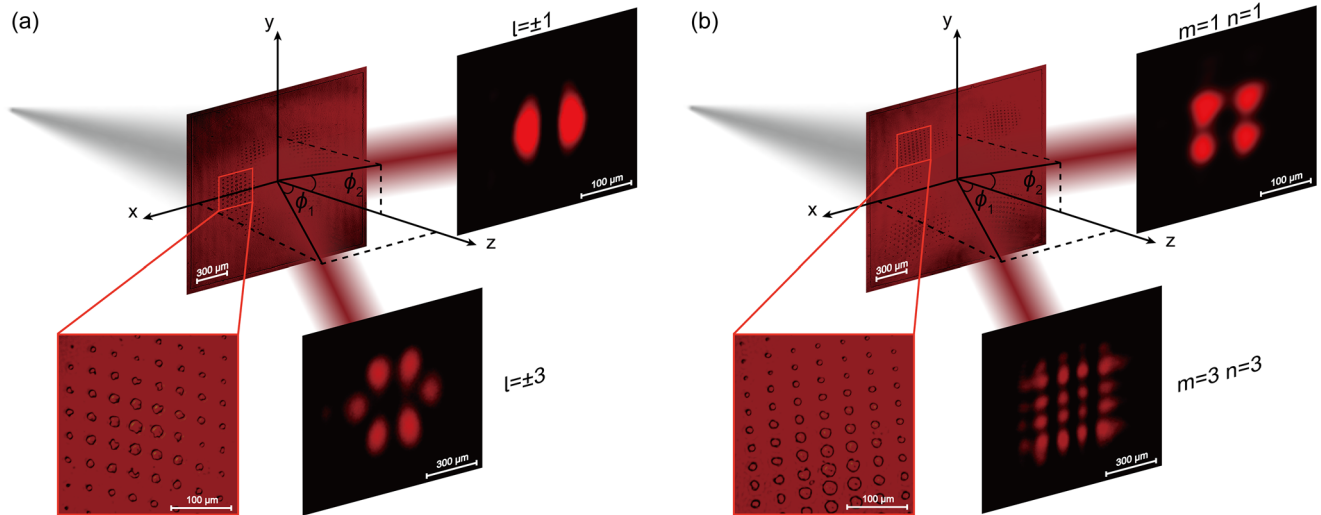
In addition to their inherent anti-noise capabilities and high fidelity, the nonlinear photon sieves allow for multi-dimensional modulation of nonlinear structured light along both the $x$ and $y$ axes. In the experimental configuration described above, Gaussian beams were selected as the incident light along the $y$-axis to ensure optimal generation of the target structured beams via the photon sieve (see Figure S7, Supporting Information). Although crosstalk arises from spatial overlap between distinct amplitude–phase distributions in the diffraction field—particularly in the case of multiplexed structured light generation—this interference is substantially mitigated when using structured beams that share the same modal profile but differ in topological order. As demonstrated in **Figure 5a**, the nonlinear photon sieve generates spatially separated superposition states of two LG beams with opposite vortex charges $l = \pm 3$, $p = 0$ and $l = \pm 1$, $p = 0$ along the $x$ and $y$ axis respectively. And HG beams with mode orders of

$m = 3$, $n = 3$ and $m = 1$, $n = 1$ can also be generated by a single photon sieve along the $x$ and $y$ axis respectively in Figure 5b. Crosstalk between co-generated structured beams, an inherent phenomenon in multi-beam structured light generation,[15,40,41] manifests as a trade-off in fidelity that can be actively tuned by adjusting the waist radii ratio. By optimizing this parameter, a balanced regime with fidelity exceeding 0.8 for both beams can be achieved (see Section S7, Supporting Information).

Meanwhile, the nonlinear process also benefits from excellent wavelength compatibility, enabling the generation of diffracted fields at different wavelengths by simply adjusting the wavelengths of the FW beam. **Figure 6** shows the SH diffracted fields of the same nonlinear photon sieves at 575 nm (Figure 6a) and 450 nm (Figure 6b), corresponding to FW wavelengths of 1150 and 900 nm, respectively. Notably, in our experiment, only the wavelength was switched while the phase pattern remained unchanged, as it was designed for $\lambda = 650$ nm. Consequently, due to the wavelength-dependence of the focal length, the focal length varies as $f'_{lens} = f_{lens} \frac{\lambda}{\lambda'}$, where $f_{lens} = 200$ mm and $\lambda = 650$ nm. When the FW wavelengths are switched to 1150 and 900 nm, the reconstructed structured light wavelengths become $\lambda' = 575$ nm and 450 nm, respectively. As a result, the focal lengths adjust to $f'_{lens} = 226$ mm and 289 nm, which is consistent with our experimental observations.

As shown in Figures 6a,b, the generated SH light fields exhibit high structural integrity and clarity. Distinct distributions of the structured light fields are clearly identifiable (see Figure S11, Supporting Information for details on determining the topological charge of the broadband LG beams). It is evident that a single pattern-poled LN slice can generate broadband diffracted fields with high fidelity across a range of incident wavelengths via the nonlinear photon sieves.

Notably, "broadband" in our context does not refer to a single beam spanning multiple wavelengths simultaneously, but to spectral tunability with consistent mode fidelity. Specifically, our nonlinear photon sieve generates target structured beams across a continuous second-harmonic range (450–650 nm) using a single, fixed design, without reconfiguration when tuning the fundamental wavelength. For each wavelength, the focal position shifts as predicted by $f'_{lens} = f_{lens} \left( \frac{\lambda}{\lambda'} \right)$, while the transverse field distribution remains consistent. Further experimental details and supporting data are provided in Section S9 (Supporting Information).

ADVANCED
SCIENCE NEWS

www.advancedsciencenews.com

LASER
& PHOTONICS
REVIEWS

www.lpr-journal.org

**Figure 5.** Generation of nonlinear structured lights with different orders by the same photon sieve. a) Superposition states of two LG beams with opposite vortex charges $l = \pm 3$, $p = 0$ along the $x$ axis and $l = \pm 1$, $p = 0$ along the $y$ axis. b) HG beams with mode orders of $m = 3$, $n = 3$ along the $x$ axis and $m = 1$, $n = 1$ along the $y$ axis.
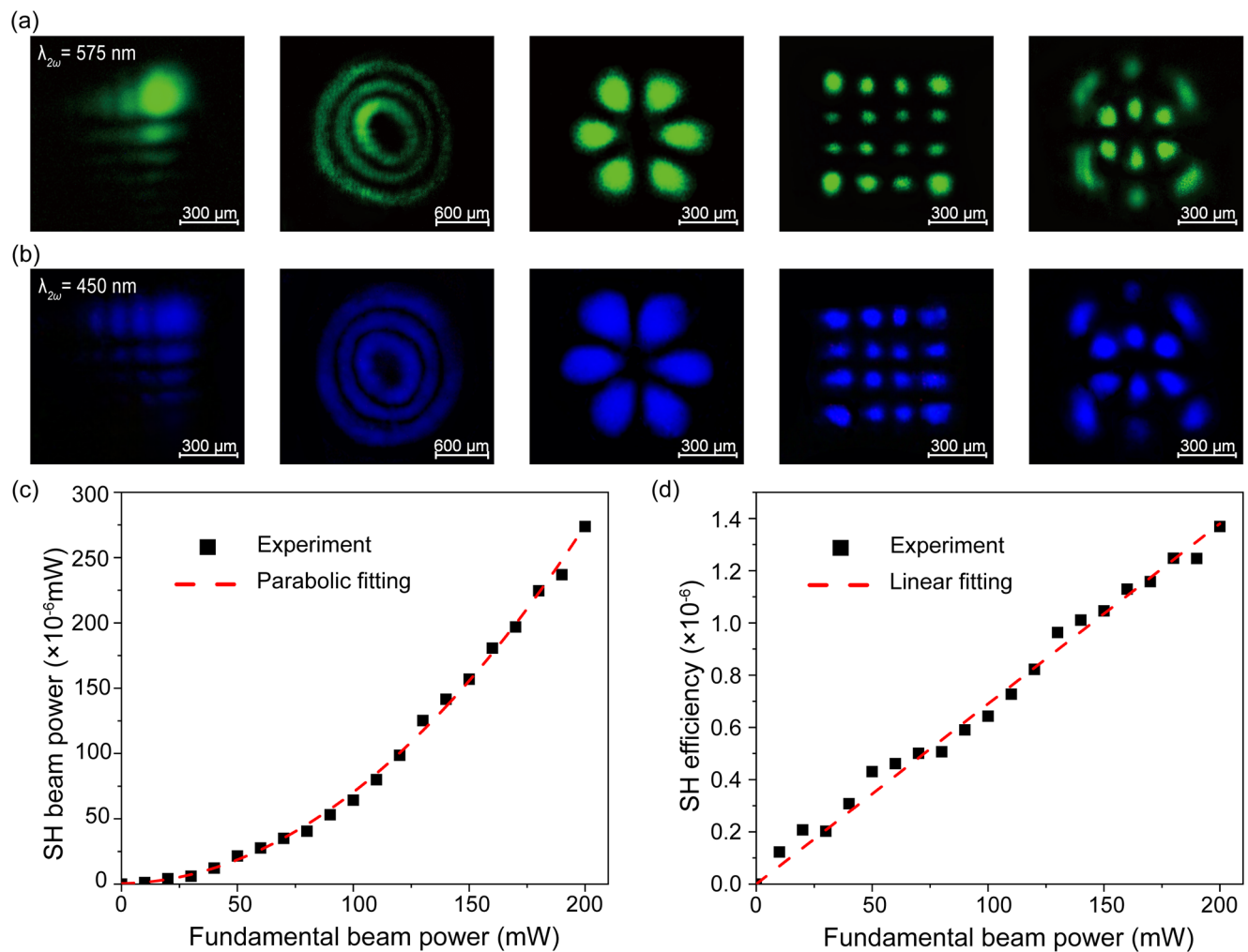


**Figure 6.** a,b) Broadband SH generation of structured light fields with FW at different NIR wavelengths of $\lambda_{FW} = 1150$ nm and $\lambda_{FW} = 900$ nm, respectively. c,d) SH beam power and nonlinear conversion efficiency as functions of pump input beam power.

By measuring the SH beam ($\lambda = 650$ nm) power, we calculate the nonlinear conversion efficiency. As shown in Figure 6c and Figure 6d, the SH beam power exhibits a quadratic dependence on the pump beam power, while the SH conversion efficiency shows a linear relationship with FW power, with an order of magnitude of $\approx 10^{-6}$. The relative low SH conversion efficiency primarily arises from longitudinal wave vector mismatch in the nonlinear Raman-Nath diffraction.[24,25] Further enhancement of SH conversion efficiency could be achieved using advanced fabrication techniques such as laser direct writing of 3D ferroelectric domains, enabling precise control of the periodic domain structure (see Section S10, Supporting Information for details).[26–31] This technology, combined with quasi-phase-matching, allows for efficient compensation of wave vector mismatches across a broader spectral range, efficiently improving the nonlinear conversion efficiency.[28]

## 5. Discussion and Conclusion

To the best of our knowledge, we present the first demonstration of a nonlinear photon sieve capable of independently and precisely controlling wavefronts of orthogonally structured light fields along the $x$ and $y$ axes. This approach exhibits high robustness against fabrication imperfections, making it a promising and versatile candidate for domain-engineered nonlinear optical crystals. By patterning the quadratic susceptibility in ferroelectric crystals utilizing this photon sieve structure, we have successfully achieved high-fidelity wavefront modulation across a broad wavelength range, as experimentally verified using electrically poled LN slices.

Although our study specifically explores nonlinear photon sieves engineered via tri-beam nonlinear holography, it further highlights the potential adaptability of analogous dot-array architectures, such as phyllotaxis-inspired nanosieves and petal-shaped photonic gears, for efficient generation and detection of multimode vortex beams.[42,43] Moreover, random dot arrays optimized with intelligent algorithms may further improve uniformity and fidelity in nonlinear optical holography,[44,45] while nonlinear photon sieves arranged into Fresnel-zone patterns could potentially function effectively as planar diffractive lenses in nonlinear optical regimes.[46,47]

Despite these advances, the conversion efficiency in electrically poled LN remains limited, primarily due to fabrication constraints. Future work will address these challenges by combining nonlinear photon sieves with advanced nanoscale domain engineering, such as 3D laser direct writing, to realize quasi-phase-matching in the sub-micron regime.[26–32] This approach could provide higher, controllable energy-conversion efficiencies, while the added flexibility of 3D domain structures may further extend the dimension of wavefront manipulation (e.g., polarization control).[31] In summary, our results highlight the potential of nonlinear photon sieves for precise wavefront shaping, represents a constructive step forward in the development of domain-engineered nonlinear optical crystals.

## Supporting Information

Supporting Information is available from the Wiley Online Library or from the author.

## Conflict of Interest

The authors declare no conflict of interest.

## Data Availability Statement

The data that support the findings of this study are available from the corresponding author upon reasonable request.

[1] H. Rubinsztein-Dunlop, A. Forbes, M. V. Berry, M. R. Dennis, D. L. Andrews, M. Mansuripur, C. Denz, C. Alpmann, P. Banzer, T. Bauer, *J. Opt.* **2017**, *19*, 013001.
[2] A. Forbes, M. de Oliveira, M. R. Dennis, *Nat. Photonics* **2021**, *15*, 253.
[3] M. Padgett, R. Bowman, *Nat. Photonics* **2011**, *5*, 343.
[4] M. Malinauskas, A. Žukauskas, S. Hasegawa, Y. Hayasaki, V. Mizeikis, R. Buividas, S. Juodkazis, *Light Sci. Appl.* **2016**, *5*, 16133.
[5] J. Wang, *Photon. Res.* **2016**, *4*, B14.
[6] R. W. Boyd, in *Nonlinear Optics*, Academic Press, San Diego, CA, **2019**.
[7] W. T. Buono, A. Forbes, *Opto-Electron. Adv.* **2022**, *5*, 210174.
[8] D. Solli, B. Jalali, *Nat. Photonics* **2015**, *9*, 704.
[9] Y. Zuo, B. Li, Y. Zhao, Y. Jiang, Y. Chen, P. Chen, G. Jo, J. Liu, S. Du, *Optica* **2019**, *6*, 1132.
[10] T. Wang, M. M. Sohoni, L. G. Wright, M. M. Stein, S. Ma, T. Onodera, M. G. Anderson, P. L. McMahon, *Nat. Photonics* **2023**, *17*, 408.
[11] Z. Yu, X. Gao, J. Yao, H. Li, Y. Shi, B. Li, Z. Xie, X. Yuan, P. Lai, Q. Song, *Adv. Mater.* **2025**, *37*, 2415142.
[12] Y. Yin, Q. Jiang, H. Wang, J. Liu, Y. Xie, Q. Wang, Y. Wang, L. Huang, *Adv. Mater.* **2024**, *36*, 2312303.
[13] H. Ahmed, M. A. Ansari, L. Paterson, J. Li, X. Chen, *Adv. Mater.* **2024**, *36*, 2312853.
[14] S. So, J. Kim, T. Badloe, C. Lee, Y. Yang, H. Kang, J. Rho, *Adv. Mater.* **2023**, *35*, 2208520.
[15] D. Wang, Y. Li, X. Zheng, R. Ji, X. Xie, K. Song, F. Lin, N. Li, Z. Jiang, C. Liu, Y. Zheng, S. Wang, W. Lu, B. Ji, Q. Wang, *Nat. Commun.* **2024**, *15*, 8242.
[16] W. Liu, Z. Li, M. A. Ansari, H. Cheng, J. Tian, X. Chen, S. Chen, *Adv. Mater.* **2023**, *35*, 2208884.
[17] G. Li, S. Zhang, T. Zentgraf, *Nat. Rev. Mater.* **2017**, *2*, 17010.
[18] B. Sain, C. Meier, T. Zentgraf, *Adv. Photonics.* **2019**, *1*, 024002.
[19] H. Chen, A. J. Taylor, N. Yu, *Rep. Prog. Phys.* **2016**, *79*, 076401.
[20] Y. Xu, *Ferroelectric Materials and Their Applications*, North-Holland, Amsterdam, **1991**.

[21] N. V. Bloch, K. Shemer, A. Shapira, R. Shiloh, I. Juwiler, A. Arie, *Phys. Rev. Lett.* **2012**, *108*, 233902.

[22] Y. Qin, C. Zhang, Y. Zhu, X. Hu, G. Zhao, *Phys. Rev. Lett.* **2008**, *100*, 063902.

[23] X. Hong, B. Yang, C. Zhang, Y. Qin, Y. Zhu, *Phys. Rev. Lett.* **2014**, *113*, 163902.

[24] Y. Liu, W. Chen, W. Zhang, C. Ma, Y. Xiong, R. Yuan, P. Chen, W. Hu, F. Xu, Y. Lu, *Adv. Optical Mater.* **2022**, *10*, 2101098.

[25] Y. Liu, W. Chen, Y. Ming, W. Zhang, J. Tang, R. Yuan, W. Hu, Y. Lu, *Las. Photonics Rev.* **2023**, *17*, 2200656.

[26] D. Wei, C. Wang, H. Wang, X. Hu, D. Wei, X. Fang, Y. Zhang, D. Wu, Y. Hu, J. Li, S. Zhu, M. Xiao, *Nat. Photonics* **2018**, *12*, 596.

[27] X. T, K. Switkowski, X. Chen, S. Liu, K. Koynov, H. Yu, H. Zhang, J. Wang, Y. Sheng, W. Krolikowski, *Nat. Photonics* **2018**, *12*, 591.

[28] D. Wei, C. Wang, X. Xu, H. Wang, Y. Hu, P. Chen, J. Li, Y. Zhu, C. Xin, X. Hu, Y. Zhang, D. Wu, J. Chu, S. Zhu, M. Xiao, *Nat. Commun.* **2019**, *10*, 4193.

[29] S. Liu, L. M. Mazur, W. Krolikowski, Y. Sheng, *Las. Photonics Rev.* **2020**, *14*, 2000224.

[30] X. Xu, T. Wang, P. Chen, C. Zhou, J. Ma, D. Wei, H. Wang, B. Niu, X. Fang, D. Wu, S. Zhu, M. Gu, M. Xiao, Y. Zhang, *Nature* **2022**, *609*, 496.

[31] P. Chen, X. Xu, T. Wang, C. Zhou, D. Wei, J. Ma, J. Guo, X. Cui, X. Cheng, C. Xie, S. Zhang, S. Zhu, M. Xiao, Y. Zhang, *Nat. Commun.* **2023**, *14*, 5523.

[32] X. Hu, Y. Zhang, S. Zhu, *Adv. Mater.* **2020**, *32*, 1903775.

[33] L. Kipp, M. Skibowski, R. L. Johnson, R. Berndt, R. Adelung, S. Harm, R. Seemann, *Nature* **2001**, *414*, 184.

[34] F. Giménez, J. A. Monsoriu, W. D. Furlan, A. Pons, *Opt. Express* **2006**, *14*, 11958.

[35] R. Liu, F. Li, M. J. Padgett, D. B. Phillips, *Optica* **2015**, *2*, 1028.

[36] J. Zhang, H. Cui, Y. Liu, X. Zhang, Y. Li, D. Zhao, Y. Zhao, Q. Zhan, *PhotoniX* **2024**, *5*, 15.

[37] H. Liu, J. Li, X. Fang, X. Zhao, Y. Zheng, X. Chen, *Phys. Rev. A* **2017**, *96*, 023801.

[38] A. Shapira, L. Naor, A. Aire, *Sci. Bull.* **2015**, *60*, 1403.

[39] M. Wang, J. Tang, H. Wang, Y. Ming, Y. Zhang, G. Cui, Y. Lu, *Appl. Phys. Lett.* **2018**, *113*, 081105.

[40] A. H. Dorrah, P. Bordoloi, V. S. de Angelis, J. O. de Sarro, L. A. Ambrosio, M. Zamboni-Rached, F. Capasso, *Nat. Photonics* **2023**, *17*, 427.

[41] Y. Wang, C. Pang, J. Qi, *Laser Photonics Rev.* **2024**, *18*, 2300832.

[42] Y. Yang, Q. Zhao, L. Liu, Y. Liu, C. Rosales-Guzmán, C. Qiu, *Phys. Rev. Appl.* **2019**, *12*, 064007.

[43] Z. Jin, D. Janoschka, J. Deng, L. Ge, P. Dreher, B. Frank, G. Hu, J. Ni, Y. Yang, J. Li, C. Yu, D. Lei, G. Li, S. Xiao, S. Mei, H. Giessen, F. M. Heringdorf, C. Qiu, *eLight* **2021**, *1*, 5.

[44] K. Huang, H. Liu, F. J. Garcia-Vidal, M. Hong, B. Luk'yanchuk, J. Teng, C. Qiu, *Nat. Commun.* **2015**, *6*, 7059.

[45] Z. Xu, Z. Huang, X. Li, C. Tang, Q. Wei, Y. Wang, *Adv. Optical Mater.* **2020**, *8*, 1901169.

[46] J. Christopher, M. Taleb, A. Maity, M. Hentschel, H. Giessen, N. Talebi, *Nanophotonics* **2020**, *9*, 15.

[47] Y. Lee, M. Low, D. Yang, H. Nam, T. D. Le, S. E. Lee, H. Han, S. Kim, Q. H. Vu, H. Yoo, H. Yoon, J. Lee, S. Sandeep, K. Lee, S. Kim, Y. Kim, *Light Sci. Appl.* **2023**, *12*, 146.